JOURNAL OF COMPUTATIONAL PHYSICS 58, 157–187 (1985)

A High-Order Godunov Scheme for Steady Supersonic Gas Dynamics

HARLAND M. GLAZ AND ANDREW B. WARDLAW

Applied Mathematics Branch, Naval Surface Weapons Center, White Oak, Silver Spring, Maryland 20910

Received September 13, 1983; revised March 7, 1984

A high-order extension of Godunov's method is developed for the equations of steady supersonic flow. Sample calculations show that the method resolves smooth flow accurately and represents strong shock waves with very little diffusion and no post-shock oscillation.

INTRODUCTION

The equations for inviscid steady supersonic flow are frequently applied to the analysis of both internal and external aerodynamic flowfields. These problems are three dimensional in nature and may exhibit complex shock systems and slip surface structures. The external flowfield about a finned missile contains the bow shock generated by the missile body, shocks produced by fin leading edges, and contact discontinuities formed at the fin trailing edges. These structures can all interact with one another, and the fins themselves may protrude through the bow shock. Internal inlet flowfields of equal complexity also occur. Here the shocks and contact discontinuities may result from the fuel injection apparatus as well as the inlet geometry itself.

Numerical solution of such aerodynamic flowfields requires an algorithm which accurately resolves, with minimum diffusion, the development and subsequent interaction of strong shock waves or slip surfaces. Two different strategies are available for treating inviscid flowfields featuring discontinuities. The most accurate results are obtained using shock fitting. Here special procedures are applied at each shock or slip surface ensuring that the resulting solution satisfies the appropriate jump conditions. This approach works well for two-dimensional flows (see [1]) but is difficult to extend to three dimensions. An algorithm can be readily designed to treat a specific three-dimensional problem with simple discontinuity structure. However, it has not proved feasible to construct a general method applicable to flowfields containing an arbitrary number of discontinuities. A second strategy for dealing with discontinuities is to capture them by differencing the equations in conservation form. This approach does not require special treatment of shocks or slip

0021-9991/85 $3.00

surfaces and is applicable to general three-dimensional flowfields. Unfortunately, this method smears out discontinuities over a number of mesh points, particularly in the case of strong shocks where extensive artificial viscosity must be added when using standard schemes. Experimentation is often required to determine the appropriate level of artificial viscosity. References [2–5] are examples of existing techniques for dealing with three-dimensional steady supersonic flowfields. Methods dependent solely on shock fitting are limited to problems with simple shock systems. Most other methods fit only certain strong shocks and capture the rest.

This paper presents a robust scheme in conservation form for treating steady supersonic flow which captures discontinuities with a minimum of diffusion and without the need to explicitly add artificial viscosity. This is achieved using an extension of Godunov's method which is higher-order accurate in regions of smooth flow. The resulting algorithm is based closely on elements of the scheme presented in [6] and [7] for unsteady gas dynamics. It can be considered to be an upwind scheme where upwinding is implemented via direct application of the characteristic equations and the Riemann problem to compute fluxes. Background on the development of this type of scheme for unsteady gas dynamics is provided in Refs. [6–10]. High-order Godunov methods are explicitly constructed to be applicable to arbitrary systems of hyperbolic conservation laws as long as the associated characteristic equations and the Riemann problem can be solved completely and efficiently.

The results presented in this paper are restricted to two-dimensional flows. However, there appear to be no major problems associated with extending this method to three dimensions. In the case of unsteady gas dynamics, this has been accomplished in Refs. [6–9], using Strang splitting with little or no loss in the sharpness of the resolved shocks and slip surfaces. A similar procedure can be applied in the case of steady supersonic flow, although other strategies are also possible.

In Section 1, the equations of motion are introduced, and the characteristic analysis for these equations is carried out. In Section 2, the Riemann problem and its numerical solution is presented. In both of these sections, the extensive analogies between unsteady gas dynamics and steady supersonic gas dynamics will be apparent. In Section 3, our high-order Godunov scheme will be constructed for initial-value problems, while boundary conditions are treated in Section 4. Finally, the numerical results for a number of model problems are presented in Section 5.

1. Equations of Motion and Characteristic Analysis

The conservation equations for steady supersonic flow, written in Cartesian coordinates, are:

$$\mathbf{F}_x + \mathbf{G}_y = 0, \tag{1}$$

where

$$\mathbf{F} = \begin{bmatrix} \rho u \\ \rho u^2 + p \\ \rho uv \\ \rho uH \end{bmatrix}; \qquad \mathbf{G} = \begin{bmatrix} \rho v \\ \rho uv \\ \rho v^2 + p \\ \rho vH \end{bmatrix}, \tag{2}$$

and x is the "marching" direction, y is the crossflow direction, u is the x-velocity component, v is the y-velocity component, ρ is the density, p is the pressure, and H is the stagnation enthalpy. For many flowfields of interest H is constant and the energy equation reduces to the constraint

$$H \equiv h(p, \rho) + \tfrac{1}{2}q^2 = H_0, \tag{3}$$

where $q^2 = u^2 + v^2$, h is the specific enthalpy, and H_0 is the constant value of H. Use of (3) in place of the energy equation introduces little loss of generality and the method discussed in this paper can be easily extended to cover the contingency of non-constant H_0. This system of equations is closed using the polytropic gas equation of state:

$$h(p, \rho) = \frac{\gamma}{(\gamma - 1)} \frac{p}{\rho}, \tag{4}$$

where $\gamma > 1$ is the ratio of specific heats. However, using the technique introduced in [8, 9] for unsteady gas dynamics, an arbitrary equation of state can be treated as well.

The system (1) may be expressed in quasilinear form as

$$\mathbf{Q}_x + \mathbf{A}\mathbf{Q}_y = 0, \tag{5}$$

where

$$\mathbf{A} = \left[\frac{\partial \mathbf{F}}{\partial \mathbf{Q}}\right]^{-1} \left[\frac{\partial \mathbf{G}}{\partial \mathbf{Q}}\right]$$

and $\mathbf{Q}$ is an arbitrary set of characteristic coordinates such that $\det[\mathbf{A}] \neq 0$. We shall consider two choices for $\mathbf{Q}$:

$$\mathbf{Q}^t = (u, v, p)', \qquad \mathbf{A}^t = (u^2 - a^2)^{-1} \begin{bmatrix} uv & -a^2 & -v/\rho \\ 0 & \frac{v}{u}(u^2 - a^2) & \frac{u^2 - a^2}{\rho u} \\ -\rho v a^2 & \rho u a^2 & uv \end{bmatrix} \tag{6a}$$

and

$$\mathbf{Q}^{II} = (p, \delta, S)^t, \qquad \mathbf{A}^{II} = (u^2 - a^2)^{-1} \begin{bmatrix} uv & \rho a^2 q^2 & 0 \\ \dfrac{q^2 - a^2}{\rho q^2} & uv & 0 \\ 0 & 0 & \dfrac{v}{u}(u^2 - a^2) \end{bmatrix}, \tag{6b}$$

where

$$S = \frac{\ln p - \gamma \ln \rho}{(\gamma - 1)}, \qquad \delta = \tan^{-1}(v/u). \tag{7}$$

Here S is a measure of the specific entropy and δ is the streamline direction. The eigenvalues of $\mathbf{A}$ are:

$$\lambda_{\pm} = \frac{uv \pm a\sqrt{q^2 - a^2}}{u^2 - a^2} \equiv \tan(\delta \pm \mu), \tag{8a}$$

$$\lambda_0 = v/u \equiv \tan \delta. \tag{8b}$$

Here, the Mach angle, μ, is given by

$$\mu = \tan^{-1}((M^2 - 1)^{-1/2}), \tag{9}$$

where the Mach number M is defined by $M^2 = q^2/a^2$, and the sound speed a is defined by $a^2 = \gamma p/\rho$.

The left and right eigenvectors of $\mathbf{A}$ are obtained by direct computation. Since $\mathbf{A}$ has distinct eigenvalues, it follows that these eigenvectors may be chosen to be bi-orthogonal, i.e., $\mathbf{l}_i \cdot \mathbf{r}_j = \delta_{ij}$ where $i, j = +, -, 0$. Defining

$$\omega = \sqrt{q^2 - a^2}, \qquad \zeta = \frac{\cot \mu}{q^2 \rho} = \frac{\omega}{a q^2 \rho} \tag{10}$$

the right and left eigenvectors for $\mathbf{A}^I$ become:

$$\begin{aligned} \mathbf{l}_0^I &= (u, v, \rho^{-1}), \\ \mathbf{l}_{\pm}^I &= \left(-v, u, \pm \frac{\omega}{\rho a}\right), \\ \mathbf{r}_0^I &= (u/q^2, v/q^2, 0)^t, \\ \mathbf{r}_{\pm}^I &= \left(\frac{\mp au - v\omega}{2q^2\omega}, \frac{\mp av + u\omega}{2q^2\omega}, \pm \frac{a\rho}{2\omega}\right)^t. \end{aligned} \tag{11}$$

Similarly for $\mathbf{A}^{II}$:

$$\begin{aligned} \mathbf{l}_0^{II} &= (\mathbf{r}_0^{II})^t = (0, 0, 1), \\ \mathbf{l}_\pm^{II} &= \tfrac{1}{2}(\pm\zeta, 1, 0), \\ \mathbf{r}_\pm^{II} &= (\pm\zeta^{-1}, 1, 0)^t. \end{aligned} \tag{12}$$

The characteristic curve given by $dy/dx = \lambda_0$ defines the streamlines of the flow-field. The curves $dy/dx = \lambda_\pm$ are the Mach lines and they represent the path of an infinitesimal disturbance. The characteristic equations are defined by $\mathbf{l} \cdot d\mathbf{Q} = 0$ for $\mathbf{l} = \mathbf{l}_{\pm,0}$ and hold along the associated characteristic curves. For $\mathbf{l} = \mathbf{l}_0$, this equation is simply $dS = 0$. Assuming isentropic flow, the Riemann invariants for steady supersonic flow may be obtained from the $\lambda_\pm$ characteristic equations. Substituting (6a) or (6b), (11) or (12), (3), and (4) into the equation $\mathbf{l} \cdot d\mathbf{Q} = 0$ and using the first law of thermodynamics, $dh = T\,dS + \rho^{-1}\,dp$, one obtains

$$d\delta \mp \cot\mu \frac{dq}{q} = 0 \tag{13}$$

or

$$dv \pm d\delta = 0 \tag{14}$$

along the curve $dy/dx = \lambda_\pm$. Here, we have introduced the Prandtl–Meyer function

$$\nu(M) = \tan^{-1}\sqrt{M^2-1} - \left(\frac{\gamma+1}{\gamma-1}\right)^{1/2} \tan^{-1}\left[\frac{\gamma-1}{\gamma+1}(M^2-1)\right]^{1/2}. \tag{15}$$

Thus, $\nu \pm \delta$ are the Riemann invariants.

Thus, we see that the characteristics and Riemann invariants for steady isentropic supersonic flow are exactly analogous to the situation for unsteady gas dynamics given in [11]. Globally, however, a characteristic curve must end whenever a sonic state is reached.

2. Elementary Waves and the Riemann Problem

The solution of the Riemann problem for (1) is self-similar in the variable y/x and consists of elementary waves. These waves may be shock waves, Prandtl–Meyer expansions, or slip-lines and they correspond in their essential features to the shock waves, rarefaction waves, and contact discontinuities, respectively, of unsteady gas dynamics. In particular, for both systems, the $\lambda_\pm$ characteristic fields are genuinely non-linear (see [12]) and the λ_0 field is linearly degenerate. Thus, an elementary $\pm$ wave is either a shock or a centered expansion, while an elementary 0-wave must be a slip-line. We will follow [13, 14] in our discussion of wave structures; this analysis is sufficient to construct an algorithm for solving the Riemann

problem. See [15] for a similar treatment and [11] for an analogous study of unsteady gas dynamics.

We introduce notation for use in the remainder of the paper. The subscripts B and T may be read as bottom and top and correspond to the usage of left and right, respectively, in the standard texts on unsteady gas dynamics [11, 12]. Plus waves face towards the top and minus waves face the bottom; the y-axis is oriented towards the top. The notation $(\mathbf{Q}_1, \mathbf{Q}_2)$ refers either to an elementary wave connecting $\mathbf{Q}_1$ on the bottom to $\mathbf{Q}_2$ on the top or the Riemann problem with $\mathbf{Q}_1$ on the bottom and $\mathbf{Q}_2$ on the top.

The three elementary waves have the following characteristics:

(i) *Slip-Lines*

The wave $(\mathbf{Q}_B, \mathbf{Q}_T)$ is a slip-line if $p_B = p_T$ and $\delta_B = \delta_T$. Thus, the wave speed (i.e., dy/dx) or inclination of the slip-line is $\lambda_0 = \delta_B = \delta_T$. The density may jump arbitrarily across a slip-line.

(ii) *Shock Waves*

Through any state $\mathbf{Q}_0$, there are two one-parameter families of states, $\tilde{S}_\pm(Q_0)$, which can be connected to $\mathbf{Q}_0$ by a shock. Here, a shock means a discontinuity which satisfies the Rankine–Hugoniot conditions for (1). The $\tilde{S}_+(\mathbf{Q}_0)$ and $\tilde{S}_-(\mathbf{Q}_0)$ curves are associated with shocks facing forwards and backwards, respectively. The projection of these curves onto the $p-\delta$ plane is illustrated in Fig. 1. The shock

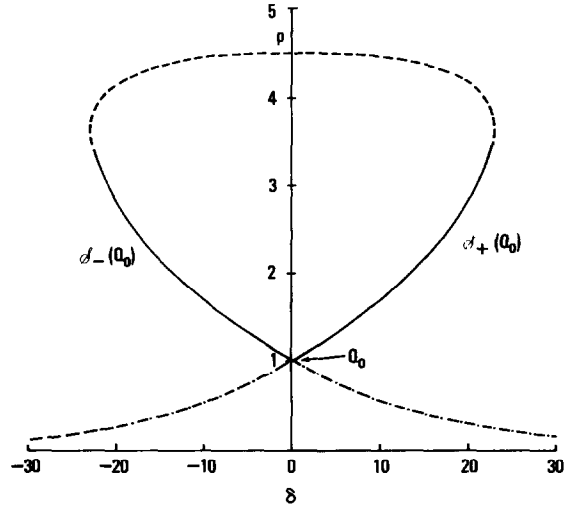

FIG. 1. The shock curves $\tilde{S}_\pm(\mathbf{Q}_0)$, $S_\pm(\mathbf{Q}_0)$ for $M_0 = 2$. Those portions of $\tilde{S}_\pm$ indicated by the dash-dotted line represent the expansion shock branch while the dashed portion represents inadmissible (i.e., $M < 1$) states which satisfy the Rankine–Hugoniot conditions. The solid lines are $S_\pm(\mathbf{Q}_0)$.

curves, $S_{\pm}(\mathbf{Q}_0)$, are defined to be the subsets of $\tilde{S}_{\pm}(\mathbf{Q}_0)$ consisting of supersonic states which satisfy the Lax entropy conditions. Thus

$S_+(\mathbf{Q}_0) = \{\mathbf{Q}$: $(\mathbf{Q}, \mathbf{Q}_0)$ satisfies the Rankine–Hugoniot conditions,
$M(\mathbf{Q}) > 1, \lambda_+(\mathbf{Q}) > \sigma > \lambda_+(\mathbf{Q}_0)\}$,

$S_-(\mathbf{Q}_0) = \{\mathbf{Q}$: $(\mathbf{Q}_0, \mathbf{Q})$ satisfies the Rankine–Hugoniot conditions,
$M(\mathbf{Q}) > 1, \lambda_-(\mathbf{Q}) < \sigma < \lambda_-(\mathbf{Q}_0)\}$,

where σ is the "shock speed," i.e., $\sigma = dy_\sigma/dx$, and $y_\sigma(x)$ is the shock path. We will refer to that portion of $\tilde{S}_{\pm}(\mathbf{Q}_0)$ for which $p < p_0$ as the "expansion shock branch." The Rankine–Hugoniot conditions may be expressed in terms of $\xi = p/p_0$ and $M_0 = q_0/a_0$:

$$\delta = \delta_0 \pm \tan^{-1}\left\{\left[\frac{\xi - 1}{\gamma M_0^2 - \xi + 1}\right]\left[\frac{2\gamma M_0^2 - (\gamma - 1) - (\gamma + 1)\xi}{(\gamma + 1)\xi + (\gamma - 1)}\right]^{1/2}\right\}, \tag{16}$$

$$\frac{\rho}{\rho_0} = \frac{(\gamma + 1)\xi + (\gamma - 1)}{(\gamma - 1)\xi + (\gamma + 1)}, \tag{17}$$

$$\frac{M}{M_0} = \left[\frac{(6\xi + 1) - 5(\xi^2 - 1)}{\xi(\xi + 6)}\right]^{1/2} \tag{18}$$

$$\beta = \pm\sin^{-1}\left[\frac{(\gamma + 1)\xi + (\gamma - 1)}{2M_0^2\gamma}\right]^{1/2}. \tag{19}$$

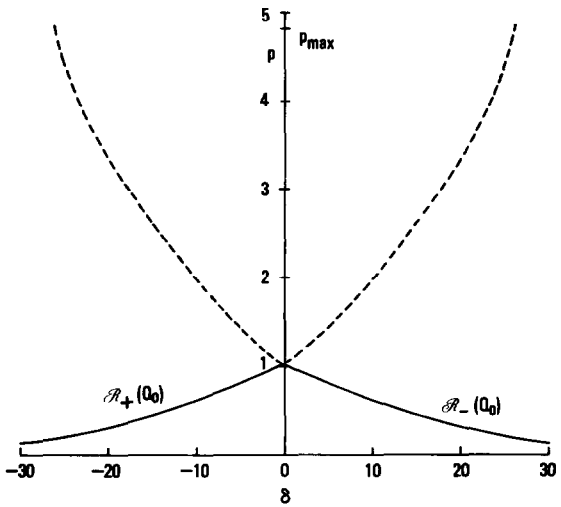

FIG. 2. The Prandtl–Meyer curves $\tilde{R}_{\pm}(\mathbf{Q}_0)$ for $M_0 = 2$. The Prandtl–Meyer expansions and compressions are denoted by solid and dashed lines, respectively. P_{max} is the isentropic compression pressure required for sonic flow.

Here, β is the angle that the shock makes with respect to the flow direction, δ_0; the $+(-)$ sign is taken for $+(-)$ shocks. It follows from the definitions that $\beta = \tan^{-1}\sigma - \delta_0$.

The Rankine–Hugoniot condition (16) implies that across a shock wave of either type,

$$\delta_B > \delta_T. \tag{20}$$

This fact is used in Section 3 as a convenient mechanism to distinguish compressions and expansions, given a large pressure jump.

(iii) *Expansion Waves*

Through any state $\mathbf{Q}_0$, there are also two one-parameter families of states $\tilde{R}_\pm(\mathbf{Q}_0)$, which can be connected to $\mathbf{Q}_0$ by a centered Prandtl–Meyer wave. Here, a Prandtl–Meyer wave is a self-similar solution of (1) in the variable y/x. As before, an $\tilde{R}_+$ wave faces forwards and an $\tilde{R}_-$ wave backwards. The projection of these curves onto the $p-\delta$ plane is illustrated in Fig. 2. The solution to these equations can be integrated using the Prandtl–Meyer function, see (15):

$$\delta(\mathbf{Q}) - \delta(\mathbf{Q}_0) = \mp[\nu(M) - \nu(M_0)], \tag{21}$$

$$M = \left\{ \frac{2}{\gamma-1}\left[\frac{1+\frac{\gamma-1}{2}M_0^2}{\xi^{(\gamma-1)/\gamma}} - 1 \right] \right\}^{1/2} \tag{22}$$

$$S = S_0, \tag{23}$$

where $\xi = p/p_0$. The Prandtl–Meyer function is monotonically increasing in M and

$$\nu(M) \to \nu_{\max} = -\frac{\pi}{2}\left[\left(\frac{\gamma+1}{\gamma-1}\right)^{1/2} - 1 \right] \quad \text{as} \quad M \to \infty;$$

also, $\nu(M) \to 0$ as $M \to 1$ and $\nu(M)$ is not defined for $M < 1$. Therefore, the Prandtl–Meyer curve can be defined only for admissible states, i.e., $M > 1$. We denote that portion of the curves $\tilde{R}_\pm(\mathbf{Q}_0)$ consisting of Prandtl–Meyer expansions (i.e., $p < p_0$) as $R_\pm(\mathbf{Q}_0)$. Therefore

$$R_+(\mathbf{Q}_0) = \{\mathbf{Q}\text{: } (\mathbf{Q}, \mathbf{Q}_0) \text{ satisfy the Prandtl–Meyer relations, } p < p_0\},$$

$$R_-(\mathbf{Q}_0) = \{\mathbf{Q}\text{: } (\mathbf{Q}_0, \mathbf{Q}) \text{ satisfy the Prandtl–Meyer relations, } p < p_0\},$$

where the Prandtl–Meyer relations are (21)–(23).

Each of the curves $\tilde{R}_\pm(\mathbf{Q}_0)$, $\tilde{S}_\pm(\mathbf{Q}_0)$ are everywhere C^∞. Furthermore, it is well known (see [13]) that $\tilde{R}_+$ and $\tilde{S}_+$, or $\tilde{R}_-$ and $\tilde{S}_-$, have second-order contact at $\mathbf{Q}_0$. We define the following composite wave curves:

$$C_\pm(\mathbf{Q}_0) = S_\pm(\mathbf{Q}_0) \cup R_\pm(\mathbf{Q}_0).$$

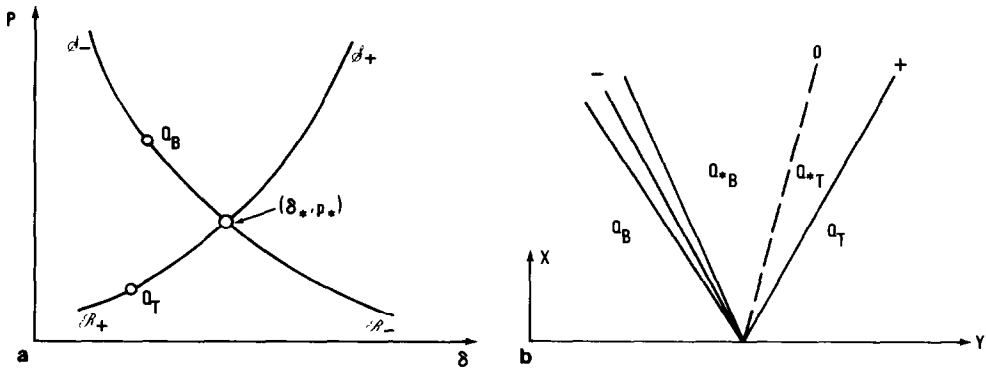

FIG. 3. The solution of the Riemann problem $(\mathbf{Q}_B, \mathbf{Q}_T)$ in the (x, y) and (p, δ) planes; $\mathbf{Q}_{*B} = (p_*, \delta_*, S_{*B})$ and $\mathbf{Q}_{*T} = (p_*, \delta_*, S_{*T})$ where S_{*B}, S_{*T} are computed by solving the jump conditions across the $\pm$ waves.

This combination satisfies the criterion that the entropy either increases (for discontinuous solutions) or remains constant (for smooth solutions) from the front to back side of any elementary wave.

The Riemann problem for steady supersonic flow is the initial value problem for (1) with initial data:

$$\begin{aligned} \mathbf{Q} &= \mathbf{Q}_T, \qquad y \geqslant 0, \\ &= \mathbf{Q}_B, \qquad y < 0. \end{aligned} \tag{24}$$

Its solution consists of a $+, 0, -$ wave in that order from top to bottom. The $\pm$ waves may be either shocks or expansions while the 0-wave is always a slip-line. In order to construct these waves, one needs to determine the intersection, (p_*, δ_*), of the curves $C_+(\mathbf{Q}_T)$ and $C_-(\mathbf{Q}_B)$ in the $p-\delta$ plane. The remaining flow properties on either side of the 0-wave can be calculated using p_* and either (17) or (22), as is appropriate. In Fig. 3, a solution is illustrated in both the $x-y$ and $p-\delta$ planes.

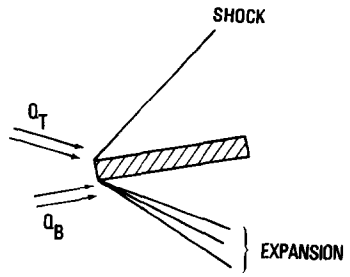

FIG. 4. Physical interpretation of the Riemann problem for steady supersonic flow. The plate is in equilibrium when the pressure on either side is equal.

Since the $C_+(\mathbf{Q}_T)$, $C_-(\mathbf{Q}_B)$ curves allow only a limited variation in δ, it is easy to construct admissible data $(\mathbf{Q}_B, \mathbf{Q}_T)$ such that $C_+(\mathbf{Q}_T) \cap C_-(\mathbf{Q}_B)$ is empty, i.e., (1), (24) has no solution. Nevertheless, we assume that any Riemann problem constructed by our difference scheme has a unique solution.

In supersonic flow, the Riemann problem has the physical interpretation illustrated in Fig. 4: given two states at the leading edge of the plate ($\mathbf{Q}_T$ associated with the top surface and $\mathbf{Q}_B$ associated with the bottom surface), determine the plate orientation which produces the same pressure, p_*, on its top and bottom surfaces, and compute p_*.

An iterative procedure is required to solve for (p_*, δ_*). We accomplish this using the secant method. A Newton iteration is also possible; see [10] for the case of unsteady gas dynamics. The iteration proceeds as follows:

$$
\begin{aligned}
&p_{*B}^{-1} = p_B, \qquad p_{*T}^{-1} = p_T,\\
&\delta_{*B}^{-1} = \delta_B, \qquad \delta_{*T}^{-1} = \delta_T,\\
&\beta_{B,T}^0 = \sqrt{(M_{B,T}^2 - 1)}/\gamma p_{B,T} M_{B,T}^2,\\
&\tilde{p}_*^0 = (\beta_T^0 p_T + \beta_B^0 p_B + \delta_B - \delta_T)/(\beta_B^0 + \beta_T^0),\\
&p_*^0 = \begin{cases} \tilde{p}_*^0, & \text{if } \tilde{p}_*^0 > 0,\\ \tfrac{1}{2}(p_B + p_T), & \text{otherwise,} \end{cases}
\end{aligned}
$$

and for $\nu = 0, 1, 2, \ldots$ to convergence:

$$
\begin{aligned}
&\xi_{B,T}^{\nu} = p_*^{\nu}/p_{B,T},\\
&M_{*B,T}^{\nu} = \left\{ \frac{2}{\gamma - 1} \left[\frac{1 + \dfrac{\gamma - 1}{2} M_{B,T}^2}{(\xi_{B,T}^{\nu})^{(\gamma-1)/\gamma}} - 1 \right] \right\}^{1/2},\\
&\delta_{*T}^{\nu} = \delta_T + \psi(\xi_T^{\nu}, M_{*T}^{\nu}; \mathbf{Q}_T),\\
&\delta_{*B}^{\nu} = \delta_B - \psi(\xi_B^{\nu}, M_{*B}^{\nu}; \mathbf{Q}_B),\\
&\beta_{B,T}^{\nu} = (\delta_{*B,T}^{\nu} - \delta_{*B,T}^{\nu-1})/(p_{*B,T}^{\nu} - p_{*B,T}^{\nu-1}),\\
&p_*^{\nu+1} = \max\left[\frac{(\beta_T^{\nu} - \beta_B^{\nu})\, p_*^{\nu} + \delta_{*B}^{\nu} - \delta_{*T}^{\nu}}{\beta_T^{\nu} - \beta_B^{\nu}}, \varepsilon \right],\\
&p_{*B}^{\nu+1} = p_{*T}^{\nu+1} = p_*^{\nu+1},
\end{aligned}
$$

where $\varepsilon \sim 10^{-6}$. The initial guess, $\tilde{p}_*^0$, consists of intersecting the tangent lines to $C_+(\mathbf{Q}_T)$, $C_-(\mathbf{Q}_B)$ at $\mathbf{Q}_T$, $\mathbf{Q}_B$, respectively. The function ψ is defined by

$$\psi(\xi, M; \mathbf{Q}_0) = \tan^{-1}\left\{\left[\frac{\xi-1}{\gamma M_0^2-\xi+1}\right]\left[\frac{2\gamma M_0^2-(\gamma-1)-(\gamma+1)\xi}{(\gamma+1)\xi+(\gamma-1)}\right]^{1/2}\right\} \quad \text{if} \quad \xi \geqslant 1,$$

$$= \nu(M_0) - \tan^{-1}(M^2-1)^{1/2} + \left(\frac{\gamma+1}{\gamma-1}\right)^{1/2} \tan^{-1}\left(\frac{\gamma-1}{\gamma+1}(M^2-1)\right)^{1/2}, \quad \text{otherwise.} \tag{25}$$

The computational effort involved in this iteration can be reduced by solving for the intersection of $\tilde{S}_+(\mathbf{Q}_T)$ and $\tilde{S}_-(\mathbf{Q}_B)$ instead of the above exact procedure. This amounts to replacing the expansion branch of $C_\pm$ with a rarefaction shock branch. As noted in [13], the resulting error in p_* is $O(\xi^3)$ and is very small in practice. To implement this scheme, eliminate the computation of $M^v_{*B,T}$ and replace ψ by

$$\phi(\xi; \mathbf{Q}_0) = \tan^{-1}\left\{\left[\frac{\xi-1}{\gamma M_0^2-\xi+1}\right]\left[\frac{2\gamma M_0^2-(\gamma-1)-(\gamma+1)\xi}{(\gamma+1)\xi+(\gamma-1)}\right]^{1/2}\right\} \operatorname{sgn}(\xi-1). \tag{26}$$

The evaluation of the solution for a particular choice of $\eta = y/x$ is straightforward unless η lies inside an expansion fan. In this case, the Mach number may be evaluated at η:

$$M = \left[1 + c^2 \tan^2\left\{\frac{\pm(\pi/2 + \nu(M_0)) - \tan^{-1}\eta}{c}\right\}\right]^{1/2} \tag{27}$$

where the $\pm$ signs correspond to $\pm$ waves, respectively, and $c = \sqrt{(\gamma+1)/(\gamma-1)}$. When using the solution of the Riemann problem in an approximate numerical scheme, it is worthwhile approximating (27) by a linear interpolation between the pre- and post-wave states. If the interpolated variables are chosen appropriately (e.g., (p, u, v)), this is an excellent approximation and the error introduced will be negligible compared to the overall truncation error of the scheme. It is important to respect the entropy condition and spread out expansion waves even when ϕ is used in place of ψ.

3. Description of the Method

Our scheme for solving the initial value problem for (1) follows directly from the schemes used by Colella [6] and Colella and Woodward [7] for unsteady gas dynamics.

The computational domain is illustrated in Fig. 5. The marching direction is x and the mesh is oriented such that $x_j^n = \text{constant} \equiv x^n$ for all j. Here n and j refer to the step number and cell number, respectively. The marching step, $\Delta x^n = x^{n+1} - x^n$, is chosen to satisfy the usual CFL condition. The computational mesh divides the

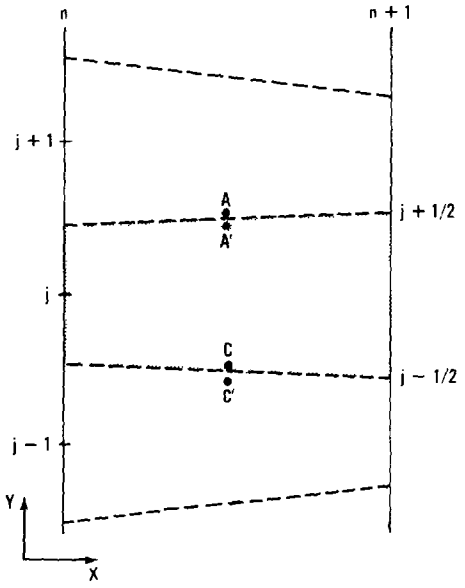

FIG. 5. The computational mesh.

computational domain into control volumes or cells which in the y-direction are centered at y_j^n and have a height of $\Delta y_j^n = y_{j+1/2}^n - y_{j-1/2}^n$.

The difference equations for the jth zone are formally derived by integrating (1) over the shaded region in Fig. 5 and applying the divergence theorem. Let $V, \partial V$ denote this region and its boundary. Then,

$$0 = \iint_V (\mathbf{F}_x + \mathbf{G}_y)\, dx\, dy = \iint_V \operatorname{div}_{(x,y)}(\mathbf{F}, \mathbf{G})\, dx\, dy = \int_{\partial V} (\mathbf{F}, \mathbf{G}) \cdot \mathbf{n}\, ds, \tag{28}$$

where $\mathbf{n}$ is the unit outward normal to ∂V. Expanding (28), we obtain

$$\mathbf{F}_j^{n+1} = \mathbf{F}_j^n \frac{\Delta y_j^n}{\Delta y_j^{n+1}} + (\mathbf{G}_{j-1/2}^{n+1/2} - s_{j-1/2}^n \mathbf{F}_{j-1/2}^{n+1/2}) \frac{\Delta x}{\Delta y_j^{n+1}} - (\mathbf{G}_{j+1/2}^{n+1/2} - s_{j+1/2}^n F_{j+1/2}^{n+1/2}) \frac{\Delta x}{\Delta y_j^{n+1}}. \tag{29}$$

Here for any quantity a:

$$a_j^n = a(y_j^n) = \int_{y_{j-1/2}^n}^{y_{j+1/2}^n} a(y, x^n)\, dy, \tag{30}$$

and

$$a_{j+1/2}^{n+1/2} = \frac{1}{\Delta x} \int_{x^n}^{x^{n+1}} a(y_{j+1/2}^n + s_{j+1/2}^n \cdot (x - x^n), x)\, dx, \tag{31}$$

where

$$s_{j+1/2}^n = (y_{j+1/2}^{n+1} - y_{j+1/2}^n)/\Delta x. \tag{32}$$

This formula is exact provided that the interface flux averages, $\mathbf{G} - s\mathbf{F}$, are known. In practice, approximate interface fluxes must be defined to complete the specification of the scheme.

In the event that the initial data at $x = x^n$ is piecewise-constant, the interface fluxes may be computed exactly by solving the Riemann problem $(\mathbf{Q}_j, \mathbf{Q}_{j+1})$ and evaluating the solution along $y/x = s_{j+1/2}$. The resulting scheme is Godunov's 1st-order method, which is outlined in [16]. The computed solution is exact for one marching step, at which point the averaging procedure, (30), destroys the detailed structure in the solution. The random choice method which is presented in [15] for steady supersonic flow fully utilizes the information in the solution to the Riemann problem. However, its extension to three-dimensional flows is problematic.

The scheme described in this paper is a generalization of Godunov's method in the sense that the interface fluxes are determined by solving Riemann problems at the upper and lower cell boundaries. However, additional steps are added to the method and instead of solving the Riemann problem $(\mathbf{Q}_j, \mathbf{Q}_{j+1})$, an approximate method of characteristics is used to define the states forming the Riemann problem. For smooth flow, the resulting fluxes are 2nd-order accurate with respect to the initial data. In the immediate vicinity of a shock, the scheme reduces to Godunov's method and the additional diffusion which is thereby introduced dampens oscillations which would be created by the 2nd-order fluxes. Since the same scheme is used in smooth and non-smooth flow (the variation from 1st- to 2nd-order is effected by a parameter), the resulting computer code efficiently vectorizes.

The algorithm for computing the interface fluxes from the initial data may be divided into a number of steps. The first of these is the "decoding" of $\mathbf{F}$ to obtain $\mathbf{Q}$, which is accomplished in a manner similar to that outlined in [3] and [4]. Given $\mathbf{F}$, define

$$\chi = \gamma^2 + (\gamma^2 - 1)\left\{\frac{F_3^2}{F_2^2} - 2H_0 \cdot \frac{F_1^2}{F_2^2}\right\}. \tag{33}$$

Then,

$$u = \frac{\gamma + \sqrt{\chi}}{\gamma + 1} \cdot \frac{F_2}{F_1},$$

$$v = F_3/F_1,$$

$$\rho = F_1/u,$$
$$p = F_2 - uF_1.$$

With $\mathbf{Q}$ known, the interface fluxes can be constructed by the following three steps.

Step 1. Construction of a piecewise-linear representation of the initial data, $\{\mathbf{Q}_j\}$. Thus,

$$q(y) = q_j + \delta q_j \cdot (y - y_j), \qquad y_{j-1/2} < y < y_{j+1/2} \tag{34}$$

for $q = q_1, q_2, q_3$, where $\mathbf{Q} = (q_1, q_2, q_3)^t$. The slopes, δq_j, are functions of the adjacent mesh values:

$$\delta q_j = \Delta(q_{j-k}, \ldots, q_{j+k}). \tag{35}$$

The numerical results presents here use a Δ with $k = 2$. Notice that for the overall scheme, $\mathbf{F}_j^{n+1} = \mathscr{F}(\mathbf{F}_{j-k-1}^n, \ldots, \mathbf{F}_{j+k+1}^n)$. The function Δ, which is specified below, is chosen to yield 4th-order spatial accuracy in smooth flow while maintaining monotonicity everywhere. This implies that the linear profiles, (34), do not introduce any new maxima or minima. A further modification is introduced near a strong shock which progressively decreases δq to zero as the shock strength increases.

Step 2. Values for $\mathbf{Q}$ are determined at each side of the midpoint of the upper and lower cell interfaces at locations denoted A, A' and C, C' in Fig. 5. This is accomplished by tracing approximate characteristics from these points back to $x = x^n$. Only those characteristics tracing back to the same zone in which the point lies are used and in general $\mathbf{Q}_A \neq \mathbf{Q}_{A'}$. Using values of $\mathbf{Q}$ at the intersection of these characteristics with $x = x^n$, values of $\mathbf{Q}$ at A, A', C, and C' are determined. When all three characteristics in a zone are of the same sign and the flow is smooth, this method reduces to the method of characteristics. After this procedure has been applied over the entire mesh, two states, denoted $\mathbf{Q}_B = \mathbf{Q}_{j+1/2,B}$ and $\mathbf{Q}_T = \mathbf{Q}_{j+1/2,T}$, are associated with each interface.

Step 3. The Riemann problem $(\mathbf{Q}_{j+1/2,B}, \mathbf{Q}_{j+1/2,T})$ is solved for each j and the solution is evaluated along $y/x = s_{j+1/2}$. This state is used to compute $\mathbf{F}_{j+1/2}$, $\mathbf{G}_{j+1/2}$.

The 1st-order Godunov scheme, by contrast, consists of decoding the conserved quantities, and executing Step 3, using the Riemann problem $(\mathbf{Q}_j, \mathbf{Q}_{j+1})$. The resulting fluxes allow the conservative variables to be advanced via (29). This method assumes property slopes are zero, eliminating the need for Steps 1 and 2.

Implementation of Steps 1 and 2 is now explored in detail. Step 3, which is the solution to the Riemann problem, has been fully covered in Section 2. The linear property profiles are determined from:

$$\delta_+ q_j = q_{j+1} - q_j; \qquad \delta_- q_j = q_j - q_{j-1}; \qquad \Delta q_j = \tfrac{1}{2}(q_{j+1} - q_{j-1}),$$

$$q_j^{\lim} = \begin{cases} 2\min(|\delta_+ q_j|, |\delta_- q_j|), & \text{if } (\delta_+ q_j)\cdot(\delta_- q_j) > 0, \\ 0; & \text{otherwise,} \end{cases}$$

$$q_j^{\mathrm{fr}} = \min(\Delta q_j, q_j^{\lim}), \tag{36}$$

$$\widetilde{\delta q_j} = \min(\tfrac{2}{3}\,|q_{j+1} - \tfrac{1}{4}q_{j+1}^{\mathrm{fr}} - q_{j-1} - \tfrac{1}{4}q_{j-1}^{\mathrm{fr}}|, q_j^{\lim}) \cdot \operatorname{sgn}(\Delta q_j),$$

$$\delta q_j = \Delta y_j \cdot \min\left(\frac{2\widetilde{\delta q_j}}{y_{j+1} - y_j}, \frac{2\delta_+ q q_j}{\Delta y_j}, \frac{2\delta_- q_j}{\Delta y_j}\right) \cdot \operatorname{sgn}(\Delta q_j) \cdot f_j.$$

Here, the notation q^{fr} refers to the "Fromm slopes" discussed in [10]. The parameter f_j, $0 \leqslant f_j \leqslant 1$, is the "slope flattening" coefficient, which is set to zero near a strong shock and is determined as follows:

$$Dp_j = p_{j+1} - p_{j-1},$$

$$\omega_j = \frac{Dp_j}{\min(p_{j-1}, p_{j+1})},$$

$$\tilde{\sigma}_j = \max(\delta_{j+1} - \delta_{j-1}, C_1 - \omega_j),$$

$$\sigma_j = \begin{cases} 1, & \text{if } \tilde{\sigma}_j \leqslant 0, \\ 0, & \text{otherwise,} \end{cases}$$

$$\beta_j = \frac{Dp_j}{Dp_{j-1} + Dp_{j+1}} = \frac{p_{j+1} - p_{j-1}}{p_{j+2} - p_{j-2}}, \tag{37}$$

$$\tilde{\tilde{f}}_j = \sigma_j \cdot \max(0, \min(C_2, C_3 \cdot (C_4 - \beta_j))),$$

$$\tilde{f}_j = \max(\tilde{\tilde{f}}_{j+1}, \tilde{\tilde{f}}_j, \tilde{\tilde{f}}_{j-1}),$$

$$f_j = 1 - \tilde{f}_j.$$

Here, C_k, $k = 1,\ldots, 4$ are adjustable parameters. For the calculations in Sections 4 and 5, we have taken $C_1 = 0.3$, $C_2 = 1.0$, $C_3 = -10.0$, and $C_4 = 0.75$. The parameter $\tilde{\sigma}_j$ checks the magnitude of the local pressure gradient and determines whether the jth zone is inside an expansion or a compression. The latter check is accomplished using the jump relation, (20). Observe that ($\beta_j \sim 1$, $\sigma_j = 1$) implies that the jth cell is inside a numerical shock layer and that the profiles within this element are flattened, i.e., $f_j \sim 0$. On the other hand, ($\beta_j \sim 0.5$, $\sigma_j = 1$) indicates that the jth cell is inside a continuous compression and that the slopes for this cell are not flattened.

We now turn to the construction of the states $\mathbf{Q}_{j+1/2,B}$ and $\mathbf{Q}_{j+1/2,T}$ located at the midpoint of the $(j, j+1)$ interface. Consider first the construction of $\mathbf{Q}_{j+1/2,B}$:

(i) Calculate the approximate characteristic directions $\lambda_{\pm,0}$ by evaluating (8) at $\mathbf{Q}_j^n$.

(ii) Trace each approximate characteristic back from the interface midpoint and determine the y-coordinates, $y_{\pm,0}$, of their intersection with $x = x^n$. Define $y_{\text{int}} = y_j + \Delta y_j/2$.

(iii) Evaluate $\mathbf{Q}_B^{\pm,0} = \mathbf{Q}(y_{\pm,0})$, using (34). Define $\mathbf{Q}_B^{\text{int}} = \mathbf{Q}_j^n + \delta\mathbf{Q}_j \cdot \Delta y_j/2$.

(iv) Calculate $\mathbf{l}_{\pm,0}^B$, $\mathbf{r}_{\pm,0}^B$ by evaluating (11) or (12) using $\mathbf{Q}_B^+$.

(v) Determine the cell edge state $\mathbf{Q}_{j+1/2,B}$ from:

$$\mathbf{Q}_{j+1/2,B} = \sum_{\mu=+,-,0} (\mathbf{l}_\mu^B \cdot \mathbf{Q}_B^\mu)\, \mathbf{r}_\mu^B, \tag{38}$$

where $\mathbf{Q}_B^\mu$ is redefined as follows:

$$\begin{aligned} \mathbf{Q}_B^\mu &= \mathbf{Q}_B^\mu \qquad \text{from (iii), if } y_\mu \leqslant y_{\text{int}}, \\ &= \mathbf{Q}_B^*, \qquad \text{otherwise,} \end{aligned}$$

and (39)

$$\begin{aligned} \mathbf{Q}_B^* &= \mathbf{Q}_B^+ \qquad \text{from (iii), if } y_+ \leqslant y_{\text{int}}, \\ &= \mathbf{Q}_B^{\text{int}}, \qquad \text{otherwise.} \end{aligned}$$

$\mathbf{Q}_{j+1/2,T}$ is calculated in an analogous manner. Here $\mathbf{Q}_T^{\text{int}} = \mathbf{Q}_{j+1}^n - \delta\mathbf{Q}_{j+1} \cdot (\Delta y_{j+1})/2$ and $\mathbf{Q}_T^\mu$ is determined from (iii) if $y_\mu \geqslant y_{\text{int}}$.

In regions of smooth flow, Steps 2 and 3 for determining cell edge fluxes $\mathbf{Q}_{j+1/2}^{n+1/2}$ are an approximation to the method of characteristics. This can be shown by considering the linearization of (1), i.e., A is a constant matrix and $\lambda_{\pm,0}$, $\mathbf{l}_{\pm,0}$, $\mathbf{r}_{\pm,0}$ are constant. Noting that $\{\mathbf{r}_\mu\}$ constitutes a basis for $\mathbf{Q}$ and that $\mathbf{l}_\mu \cdot \mathbf{r}_\nu = \delta_{\mu\nu}$ for $\mu, \nu = +, 0, -$, it follows that the projection of an arbitrary vector $\mathbf{Q}$ onto the subspace spanned by $\mathbf{r}_\mu$ is simply $(\mathbf{l}_\mu \cdot \mathbf{Q})\, \mathbf{r}_\mu$. Therefore,

$$\mathbf{Q} = \sum_{\mu=+,0,-} (\mathbf{l}_\mu \cdot \mathbf{Q})\, \mathbf{r}_\mu. \tag{40}$$

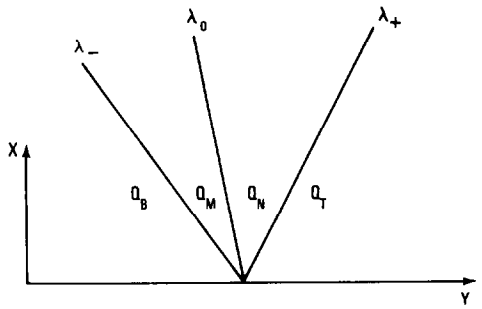

FIG. 6. Solution of the Riemann problem for the linearization of system (1).

The solution of the Riemann problem for this situation is shown in Fig. 6. Using the notation from this figure and defining $\alpha_\mu = (\mathbf{Q}_T - \mathbf{Q}_B)\cdot \mathbf{l}_\mu$, its solution can be expressed as:

$$\begin{aligned} \mathbf{Q}_T &= \mathbf{Q}_B + \sum_{\mu = +,0,-} \alpha_\mu \mathbf{r}_\mu, \\ \mathbf{Q}_m &= \mathbf{Q}_B + \alpha_- \mathbf{r}_-, \\ \mathbf{Q}_n &= \mathbf{Q}_m + \alpha_0 \mathbf{r}_0. \end{aligned} \tag{41}$$

Now suppose that $\lambda_+, \lambda_0 \geqslant s_{j+1/2}$ and $\lambda_- < s_{j+1/2}$ as illustrated in Fig. 7a. From the scheme of (38) and (39) we get:

$$\begin{aligned} \mathbf{Q}_{j+1/2,B} &= (\mathbf{l}_+ \cdot \mathbf{Q}_B^+)\,\mathbf{r}_+ + (\mathbf{l}_0 \cdot \mathbf{Q}_B^0)\,\mathbf{r}_0 + (\mathbf{l}_- \cdot \mathbf{Q}_B^+)\,\mathbf{r}_-, \\ \mathbf{Q}_{j+1/2,T} &= (\mathbf{l}_+ \cdot \mathbf{Q}_T^-)\,\mathbf{r}_+ + (\mathbf{l}_0 \cdot \mathbf{Q}_T^-)\,\mathbf{r}_0 + (\mathbf{l}_- \cdot \mathbf{Q}_T^-)\,\mathbf{r}_-. \end{aligned} \tag{42}$$

The solution of the Riemann problem $(\mathbf{Q}_{j+1/2,B}, \mathbf{Q}_{j+1/2,T})$ evaluated at $y/x = s_{j+1/2}$ is $\mathbf{Q}_m$, i.e.,

$$\mathbf{Q}_{j+1/2}^{n+1/2} = (\mathbf{l}_+ \cdot \mathbf{Q}_B^+)\,\mathbf{r}_+ + (\mathbf{l}_0 \cdot \mathbf{Q}_B^0)\,\mathbf{r}_0 + (\mathbf{l}_- \cdot \mathbf{Q}_T^-)\,\mathbf{r}_-. \tag{43}$$

On the other hand, the method of characteristics consists of solving $\mathbf{l}_\mu \cdot d\mathbf{Q} = 0$ along $dy/dx = \lambda_\mu$ for $\mu = \pm, 0$. Noting that $\mathbf{l}\cdot d\mathbf{Q} = d(\mathbf{l}\cdot\mathbf{Q})$ for a linear system and

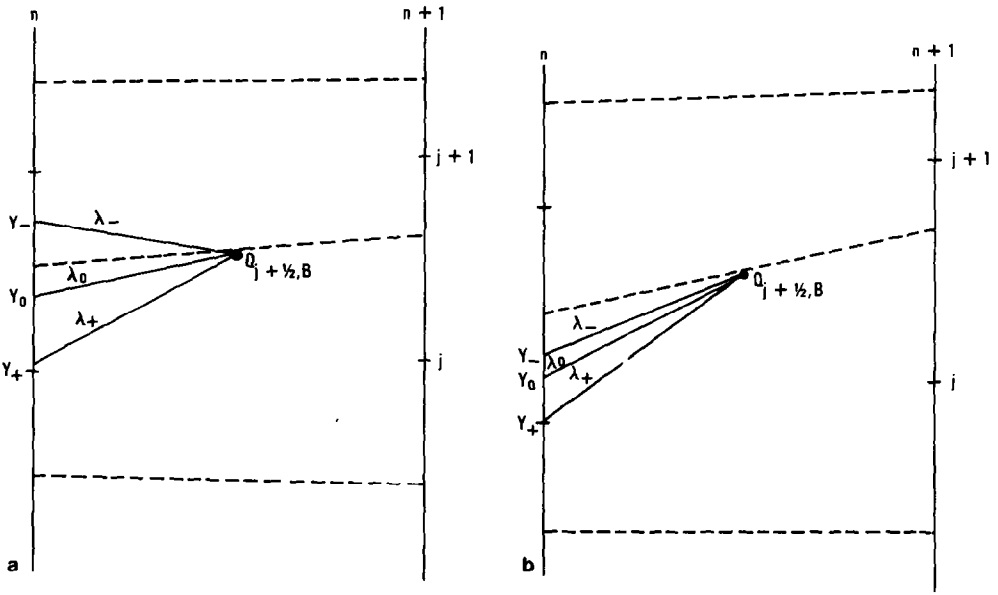

FIG. 7. Tracing characteristics from $\mathbf{Q}_B = \mathbf{Q}_{j+1/2,B}$; (a) subsonic crossflow, (b) supersonic crossflow.

approximating $d\mathbf{Q} \sim \mathbf{Q}_{j+1/2}^{n+1/2} - \mathbf{Q}^{\mu}$ where $\mathbf{Q}^{\mu} = \mathbf{Q}(y_{\mu}, x^n)$ and y_{μ} may lie in either cell j or $j+1$ leads directly to (43).

In the case $\lambda_+, \lambda_0, \lambda_- \geqslant s_{j+1/2}$ shown in Fig. 7b, (38) and (39) yield:

$$\begin{aligned} \mathbf{Q}_{j+1/2,B} &= (\mathbf{l}_+ \cdot \mathbf{Q}_B^+)\,\mathbf{r}_+ + (\mathbf{l}_0 \cdot \mathbf{Q}_B^0)\,\mathbf{r}_0 + (\mathbf{l}_- \cdot \mathbf{Q}_B^-)\,\mathbf{r}_-, \\ \mathbf{Q}_{j+1/2,T} &= \mathbf{Q}_T^{\text{int}}. \end{aligned} \tag{44}$$

The solution of the Riemann problem for $(\mathbf{Q}_{j+1/2,B}, \mathbf{Q}_{j+1/2,T})$ evaluated at $y/x = s_{j+1/2}$ is $\mathbf{Q}_{j+1/2,B}$ which is identical to the method of characteristic solution.

Analysis of the remaining two cases, $\lambda_+ > s_{j+1/2}$, λ_-, $\lambda_0 \leqslant s_{j+1/2}$ and λ_-, λ_0, $\lambda_+ \leqslant s_{j+1/2}$ follow directly from the above arguments.

4. Boundary Conditions

The calculations presented in this paper represent duct flows and the only boundary condition which arises is that associated with an impermeable wall. At the wall, the velocity vector must be tangent to the wall. The computational mesh employed near a wall is illustrated in Fig. 8. The cell edge nearest to the wall lies along the wall while the mesh point closest to the wall is located half a cell width from the wall. If $b^n = y_{1/2}^n$ denotes the bottom wall location at $x = x^n$, then the wall slope is defined by the finite difference expression

$$b_x^n = (b^{n+1} - b^n)/(x^{n+1} - x^n). \tag{45}$$

A similar expression defines the top wall.

Near a well, $\mathbf{F}$ is advanced using (29) and the interface fluxes are calculated using basically the same three-step procedure applied to interior zones. However, a few

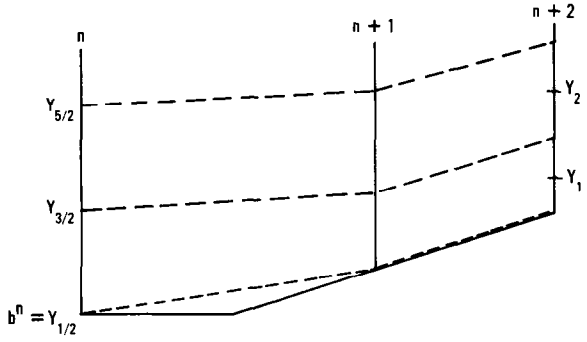

Fig. 8. The computational mesh at the bottom boundary. The dashed line indicates the effective mesh.

modifications are required. The following expressions are used to calculate δq_i at the bottom wall:

$$\begin{aligned} \delta q_2 &= q_j^{\text{fr}} f_2, \\ \widetilde{\delta q}_1 &= -1.5q_1 + 2q_2 - 0.5q_3, \\ \delta q_1 &= \min(|\widetilde{\delta q}_1|, q_2^{\text{lim}}) \operatorname{sgn}(\widetilde{\delta q}_1) f_1. \end{aligned} \tag{46}$$

The shock detection parameter, f_j, is also redefined:

$$\begin{aligned} f_2 &= 1.0 - \max(\tilde{\tilde{f}}_3, \sigma_2), \\ f_1 &= 1 - \sigma_2. \end{aligned} \tag{47}$$

Analogous expressions are used near the top wall. Steps 2 and 3 of the interior scheme remain the same except at the wall. Here, the state $\mathbf{Q}_{1/2,T}^{n+1/2}$ is computed as before and then the state $\mathbf{Q}_{1/2}^{n+1/2}$ at the wall is specified by turning $\mathbf{Q}_{1/2,T}^{n+1/2}$ tangent to the wall by either a + shock wave or Prandtl–Meyer expansion depending on which direction the flow is required to turn. In the event that $\delta q_1 = 0$, it is easy to see that this procedure is equivalent to reflecting $\mathbf{Q}_1$ across the wall forming $\mathbf{Q}_0$, solving the Riemann problem $(\mathbf{Q}_0, \mathbf{Q}_1)$, and evaluating its solution at $y/x = b_x^n$. By reflection, we mean that

$$p_0 = p_1, \qquad \rho_0 = \rho_1, \qquad q_0 = q_1, \qquad \delta_0 = 2\theta - \delta_1,$$

where $\theta = \tan^{-1}(b_x^n)$.

As will be demonstrated, this boundary treatment yields satisfactory results except in the presence of wall slope discontinuities. Such discontinuities turn the flow at the wall through either a compression or an expansion. A compression turn generates a shock wave which propagates into the flowfield while an expansion turn produces a Prandtl–Meyer expansion. The actual location of such a discontinuity generally falls in the middle of a marching step, as illustrated in Fig. 8. Since the wall slope is described by (45), the discontinuity is simulated by two successive discontinuous turns; this alters the geometry of the problem being considered and, therefore, its analytic solution.

To circumvent this problem and to more accurately resolve the flow in the neighborhood of slope discontinuities requires a special treatment of the numerical boundary conditions. Separate procedures have been developed for compression and expansion turns.

Compression Discontinuities

Numerical results for the interaction of a uniform free stream with a sharp compressive 30° turn are presented in Fig. 9. Using the boundary procedure outlined above, the pressure at the wall is nearly correct but there is a very large error in wall density and, consequently, in the location of the numerical shock layer. This error is due in large part to the application of two successive turns rather than the

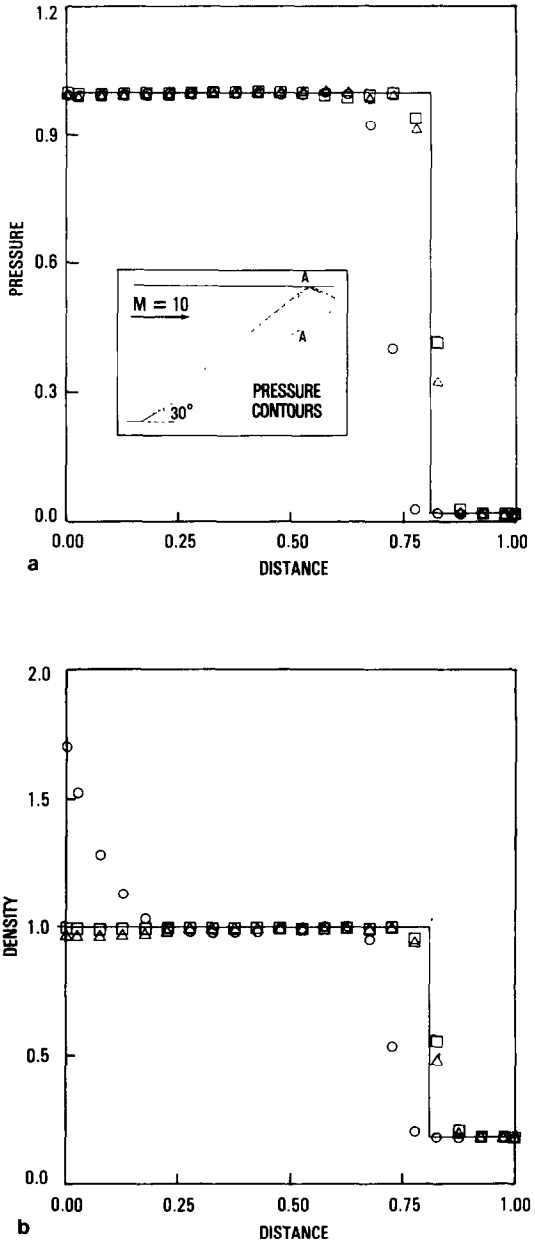

FIG. 9. The inset is the computed pressure contours for a Mach 10, 30° compressive turn using the high-order scheme with the special boundary treatment. The results are for section $A-A$. ○, basic scheme; △, hit the turn exactly; □, special procedure; solid line, exact solution.

one intended, thereby producing an incorrect value for entropy downstream of the turn. Since the wall is a streamline, this error persists forever. In Ref. [17] the analogous phenomena occurred at solid walls in unsteady gas dynamics. In both cases, the error arises from attempting to specify boundary treatments at boundaries which are also linearly degenerate (i.e., λ_0) characteristics. This issue is discussed in Ref. [18].

A simple remedy for this problem is to adjust the step size to ensure that a turn coincides with the end of a step and this greatly reduces the density error as is illustrated in Fig. 9. However, examples have been computed where the residual error is still as large as 5–10%.

The following heuristic procedure, applied following the slope discontinuity and in conjunction with the step size adjustment, has been found to lead to accurate results:

(1) At the completion of each step, check for the occurrence of a wall slope discontinuity. If one occurs, record the state of the wall cell, $\mathbf{Q}_u$, which is representative of conditions immediately upstream of the turn. Let $\mathbf{Q}_f$ be the state obtained by turning $\mathbf{Q}_u$ until it is tangent to the local wall slope downstream of the turn.

(2) Downstream of the wall slope discontinuity, the wall fluxes are computed using the state $\mathbf{Q}_f$.

(3) At the completion of each step, the location of the outer edge of the wall cell is compared to the position of the shock wave which originates at the wall slope discontinuity with inclination β relative to the streamline of the state $\mathbf{Q}_u$. If the cell edge is located between the shock and the wall, the state $\mathbf{Q}_f$ is assigned to this cell and the special procedure is terminated.

The number of steps for which the special procedure is in effect depends on Mach number and the magnitude of the turn, but it is typically on the order of 2–6 steps.

Expansion Turns

In this case, simulating a discontinuity in two successive steps has little effect on the downstream entropy since expansions are isentropic. Nevertheless, the accurate computation of the downstream flowfield requires a step size adjustment at wall slope discontinuities as above. Results are further improved by applying the following special procedures:

(1) At the end of each step, check for a wall slope discontinuity and if one occurs, store the wall state, $\mathbf{Q}_u$, upstream of the turn.

(2) At the completion of each step downstream of the turn, compute the angle, θ, of the line intersecting the discontinuity point and the center of the wall cell, with respect to the streamline direction of state $\mathbf{Q}_u$. Construct the Prandtl–Meyer expansion formed by turning state $\mathbf{Q}_u$ to the local wall slope. Compute the conditions along the characteristic of orientation θ with respect to the undisturbed flow streamlines and assign this state to the first cell.

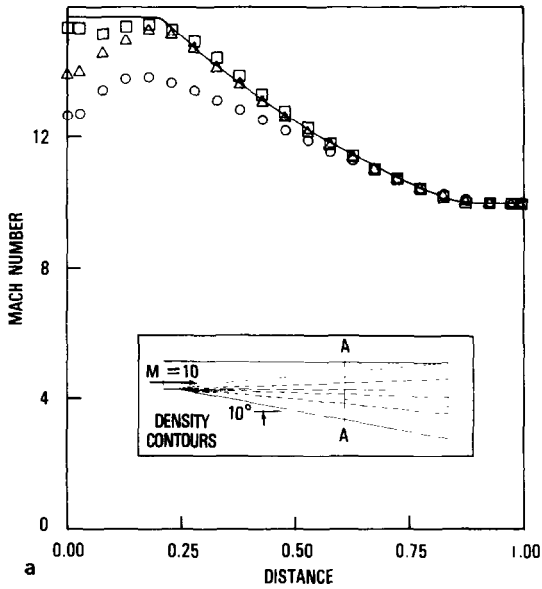

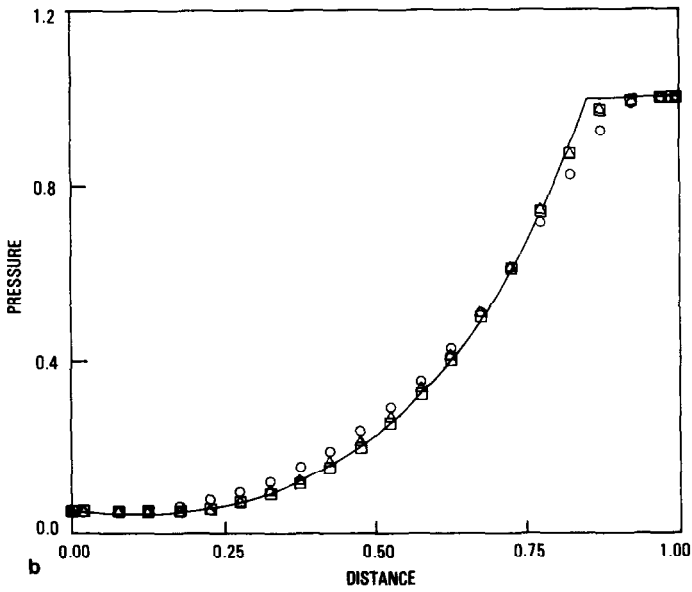

FIG. 10. The inset is the computed density contours for a Mach 10, 10° expansion turn using the high-order scheme with the special boundary treatment. The results are for section $A-A$. ○, 1st-order scheme, turn hit exactly; △, 2nd-order scheme, turn hit exactly; □, 2nd-order scheme, special procedure; solid line, exact solution.

(3) Terminate the special procedure when the characteristic direction, θ, falls in the constant property region behind the Prandtl–Meyer expansion.

Figure 10 presents results for a Prandtl–Meyer expansion using an adjusted step size in conjunction with the 1st-order Godunov scheme, the 2nd-order scheme, and the 2nd-order scheme combined with the above special procedure. Best agreement with the analytic solution is obtained with the latter scheme although a 6% error in Mach number remains near the wall. This represents a substantial improvement over the other two calculations. Worst results are obtained with the 1st-order scheme where truncation error exacerbates the situation at the boundary.

5. Results

A number of examples are computed to illustrate the ability of the high-order Godunov method to accurately resolve smooth flows as well as those containing discontinuities. Calculations have been carried out using 20 points in the first two examples and 50 in the final three cases. Improved solutions could have been obtained using more computational points; however, such meshes are not practical for multidimensional problems and hence are not considered. All of the examples were computed using a step size which was 90% of the allowable step size based on the CFL condition. Calculations have been carried out using both $\mathbf{Q}^I$ and $\mathbf{Q}^{II}$ as dependent variables. Results from these two approaches are nearly identical and the exhibited solutions in this section were computed using $\mathbf{Q}^I$.

Computed and exact solutions for source flow are considered in Figs. 11 and 12 using the illustrated geometry. In this example fluid emanates from a point source and expands in a radially symmetric pattern. The flow is isentropic and has a constant stagnation enthalpy. Using these constraints in conjunction with the perfect gas equation of state and mass conservation produces the following relation for ρ:

$$\frac{\gamma}{(\gamma-1)}\exp[S(\gamma-1)]\,\rho^{\gamma+1}r^2+\frac{\tilde{M}^2}{2}-H_0\rho^2r^2=0.$$

Here r is the radial distance from the source and $2\pi\tilde{M}$ is the mass flux from the source. This equation must be solved iteratively except in the case $\gamma=3$. Calculated results for the Godunov and high-order Godunov schemes are shown in Figs. 11 and 12, respectively. Initial conditions are prescribed at $x=1$ and feature a Mach number slightly greater than two while the illustrated results are at $x=20$. The computed results for the high-order Godunov method are significantly more accurate than those obtained with the Godunov approach.

The second example considered is flow through an "S"-shaped duct. The duct was specifically designed to expand uniform initial flow to uniform conditions in the middle of the "S" turn and then to compress the flow back to its original state. The geometry of the lower duct wall through the expansion section is specified while the

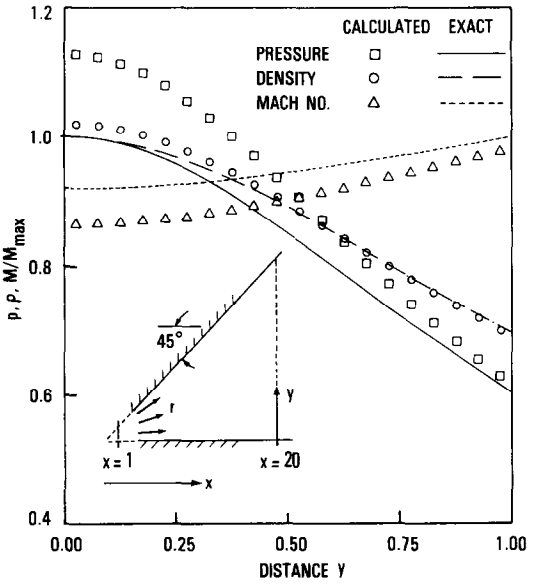

FIG. 11. Computed source flow results with the 1st-order scheme.

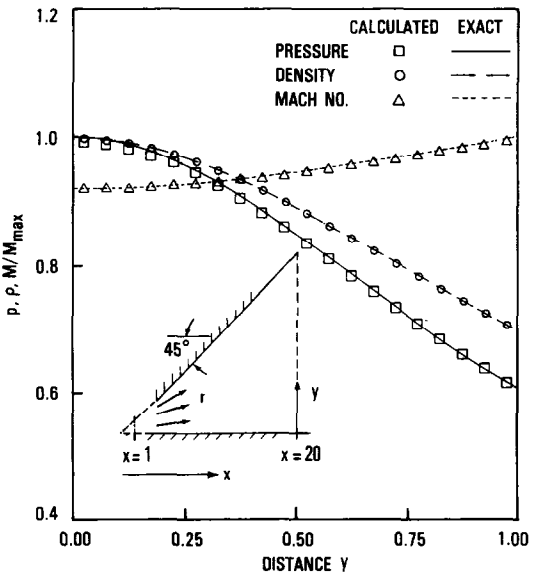

FIG. 12. Computed source flow results with the 2nd-order scheme.

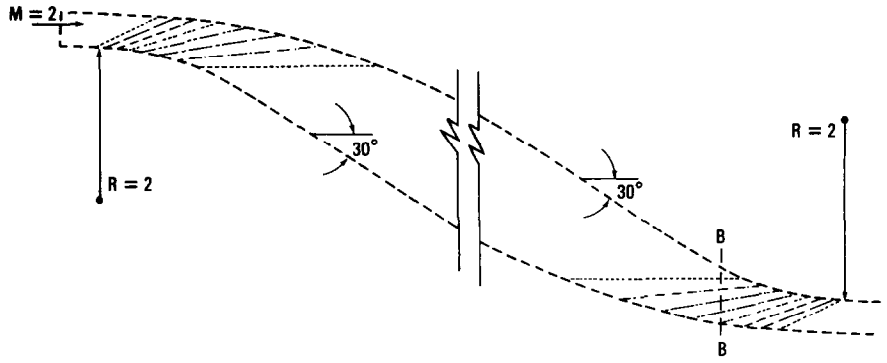

FIG. 13. Pressure contour plot of the entrance and exit sections of a symmetric S-shaped duct.

upper wall profile is determined using a characteristic analysis. Entering the expansion turn, characteristics generated at the lower wall are traced to their intersection point with the upper wall and the upper wall slope is then adjusted so that it is parallel with the flow direction defined along the characteristic. The roles of the upper and lower walls are reversed in the compression section of the duct. The resulting flow field features characteristics which are straight lines. A contour plot of pressure computed by the high-order scheme is shown in Fig. 13, and constant

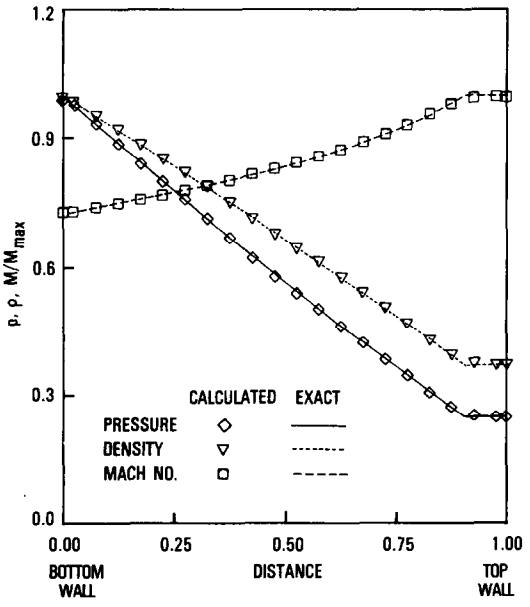

FIG. 14. Computed and exact property profiles at section $B-B$ of the S-shaped duct.

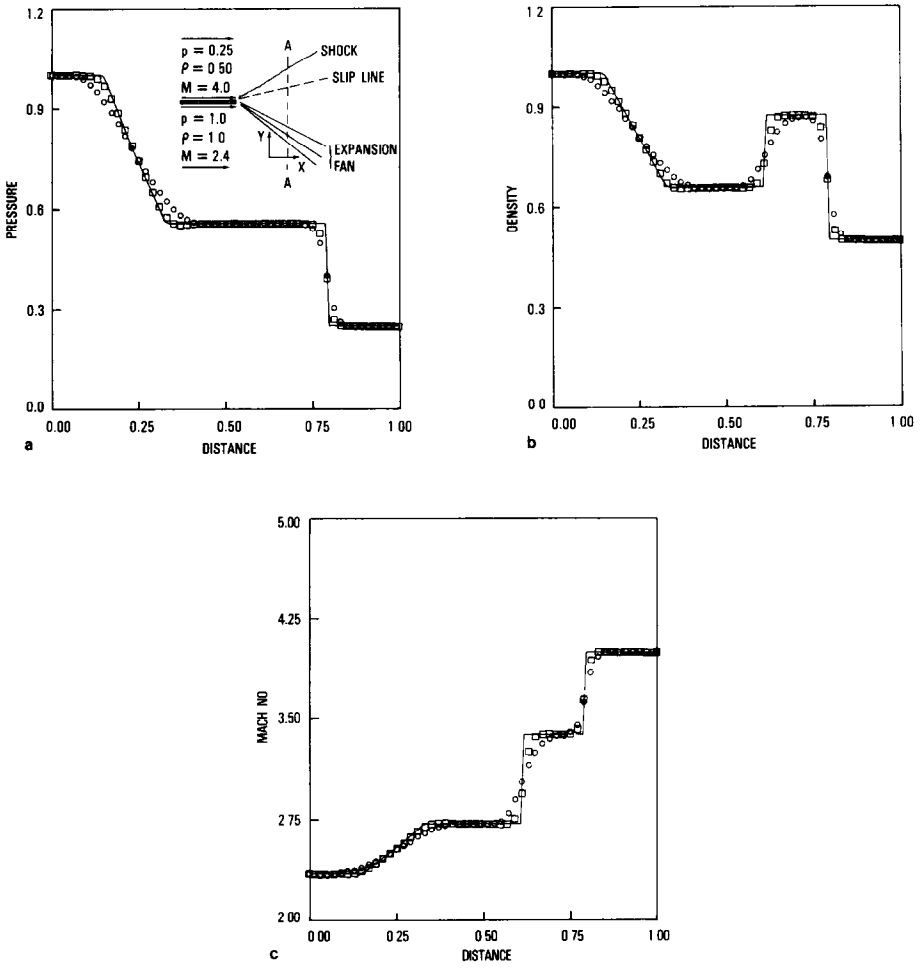

FIG. 15. The exact solution, 1st-order scheme results, and 2nd-order scheme results for the Riemann problem defined in the inset. ○, 1st-order results; □, 2nd-order results; solid line, exact solution.

pressure contours are approximately straight lines in both the expansion and compression turns. Property values along section $B-B$ of Fig. 13 are illustrated in Fig. 14 and are in excellent agreement with the analytic solution.

Two Riemann problems are considered in Figs. 15 and 16. The first is formed by the confluence of two parallel streams with different states. The jump in pressure, density, and Mach number across these two streams is 4, 2, and $\frac{5}{3}$, respectively. The resulting interaction produces a shock which propagates into the low-pressure fluid and an expansion which propagates into the high-pressure region. The resulting density jump across the contact discontinuity is $\frac{4}{3}$. Throughout the interaction

between these two streams, the crossflow is subsonic (i.e., $v/a \leqslant 1$). Results for both the Godunov and high-order Godunov schemes at section $A-A$ are shown in Fig. 15 along with the exact solution which was generated using the analysis of Section 2. The high-order Godunov scheme provides a sharper description of the shock and the contact discontinuity as well as a more accurate representation of the expansion. The shock and contact discontinuities appear to be captured in two points.

A Riemann problem formed by two intersecting streams is shown in Fig. 16. Here, the angle of intersection between the two streams is 23° while the pressure, density, and Mach number jumps across the two streams are 100, 20, and 2.86, respectively. The resulting interaction again features a shock propagating into the low-pressure stream and an expansion traveling into the high-pressure region. Below the shock the crossflow is supersonic and the high-order Godunov method method for determining cell edge fluxes reduces to a method of characteristics. Calculated results, which are shown in Fig. 16, are in reasonable agreement with the analytic solution for the Riemann problem. However, the contact discontinuity appears to be smeared over more points than in the previous example and an undershoot in pressure and density occurs at the foot of the expansion. The expansion undershoot is principally caused by starting error and can be eliminated by using initial data which cover the expansion with 5 to 10 points. It can also be

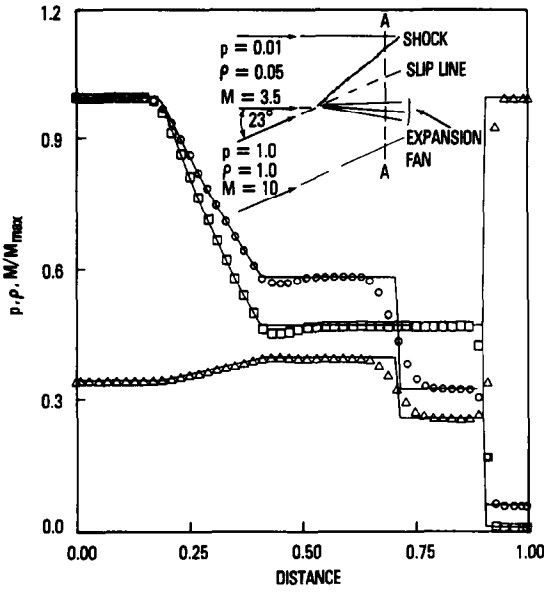

FIG. 16. The exact solution and numerical results with the 2nd-order scheme for the Riemann problem defined in the inset. ○, Computed density; □, computed pressure; △, computed Mach number; solid lines, exact solutions for these quantities.

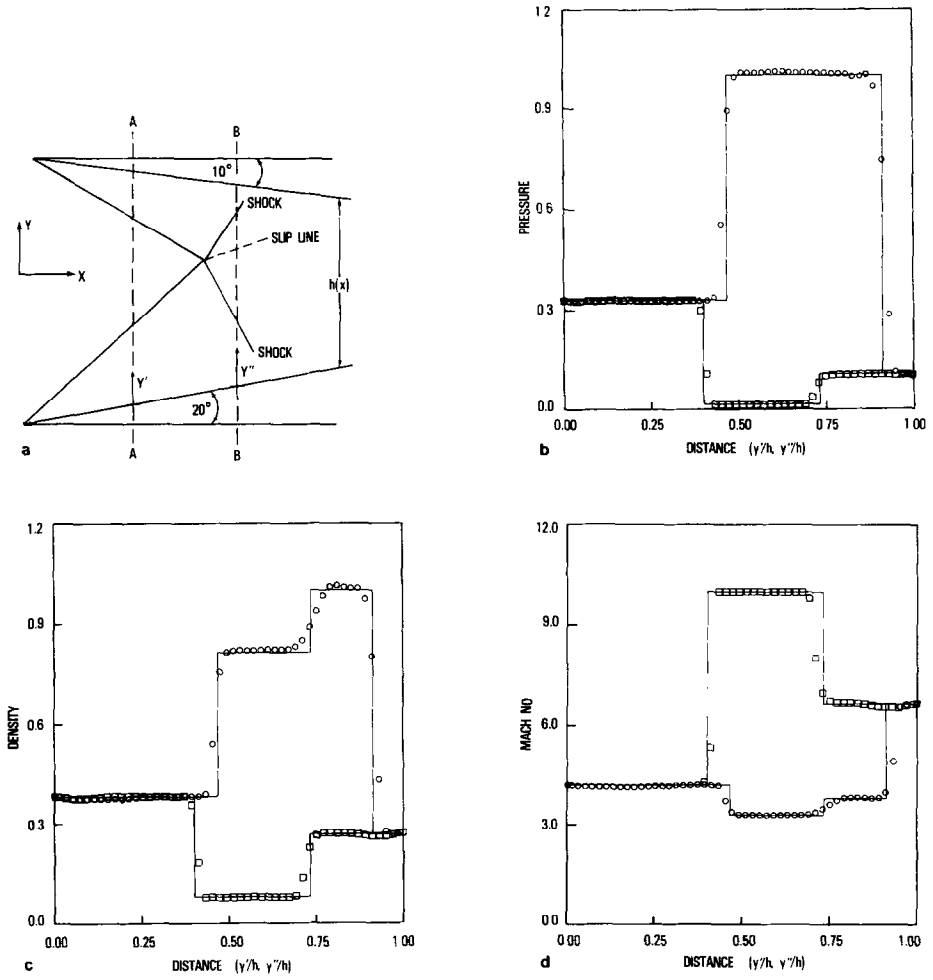

FIG. 17. The exact solutions and numerical results with the 2nd-order scheme for the shock interaction problem defined in (a). ○, Results at section $B-B$; □, results at section $A-A$. Solid lines are the exact solutions.

reduced by increasing the number of points used in the calculation or by starting the problem using an extremely small step size.

A shock interaction example is illustrated in Fig. 17 which is generated by a duct containing both an upper and lower wall slope discontinuity. These produce two shocks which move towards the center of the duct and interact to form two reflected shocks and a contact discontinuity. The exact solution to this problem can be constructed using the results for shock waves presented in Section 2 to predict the locations and strengths of the shock induced by the upper and lower wall slope dis-

continuities. The resulting interaction of these two shocks is determined using the solution to the equivalent Riemann problem. Figure 17 illustrates computed property values at sections $A-A$ and $B-B$. The first of these is upstream of the shock interaction and shows the two shocks generated by the upper and lower slope discontinuities. The second section is downstream of the shock interaction and illustrates the reflected shocks as well as the contact discontinuity. The computed shocks are appropriately located in both sections and are captured in two points while the contact discontinuities are captured in four to five points.

To place the high-order Godunov results in perspective, comparison computations have been carried out using MacCormack's method, see [19], in conjunction with a Schuman filter, see [20]. The Schuman filter, applied with a density switch, adds smoothing which is necessary to capture strong shocks. The MacCormack algorithm and Schuman filter are described for a uniform mesh by:

$$\text{predictor: } \bar{\mathbf{F}}_j = \mathbf{F}_j^n - (\mathbf{G}_j^n - \mathbf{G}_{j-1}^n)\,\Delta x/\Delta y,$$

$$\text{corrector: } \mathbf{F}_j^c = \tfrac{1}{2}(\mathbf{F}_j^n + \bar{\mathbf{F}}_j) - \tfrac{1}{2}(\bar{\mathbf{G}}_{j+1} - \bar{\mathbf{G}}_j)\,\Delta x/\Delta y,$$

$$\text{filter: } \mathbf{F}_j^{n+1} = \mathbf{F}_j^c + D_{j+1/2}(\mathbf{F}_{j+1}^c - \mathbf{F}_j^c) - D_{j-1/2}(\mathbf{F}_j^c - \mathbf{F}_{j-1}^c),$$

where

$$D_{j+1/2} = [(\bar{\rho}_{j+1} - \bar{\rho}_j)/(\bar{\rho}_{j+1} + \bar{\rho}_j)]\,\bar{D}$$

and $\bar{D}$ is an adjustable constant. This scheme is currently one of the most widely applied algorithms for computing inviscid aerodynamic flowfields. It has been implemented using the same control volume formulation applied in the high-order Godunov calculations. Wall fluxes in both the predictor and corrector steps are computed by turning the flow at the cell adjacent to the wall through the appropriate shock or expansion.

The performance of MacCormack's method is very problem dependent. In the case of a simple compression ramp, shocks with pressure jumps of 7 to 1 and 22 to 1 were captured in 2 to 3 points without the use of smoothing. However, in more complicated problems, significant smoothing was necessary to damp oscillations in the vicinity of shocks. Figure 18 illustrates the computed pressure for the shock interaction example described in Fig. 17, using moderate levels of smoothing ($\bar{D} = 0.5$). The pressure oscillations visible near the shock can be damped using higher levels of smoothing, but at the expense of additional shock smearing.

An extensive comparison of the performance of several schemes for unsteady gas dynamics, including MacCormack's scheme and high-order Godunov schemes, applied to shock interaction problems in one and two space dimensions has been reported in Ref. [21]. Although the high-order Godunov schemes cost about six times as much computer time per mesh point as the MacCormack scheme in the reported calculations (and this is also the case for the schemes applied to the equations of steady supersonic flow), it is nevertheless the case that the high-order Godunov scheme proved to be more efficient in terms of required computer time to

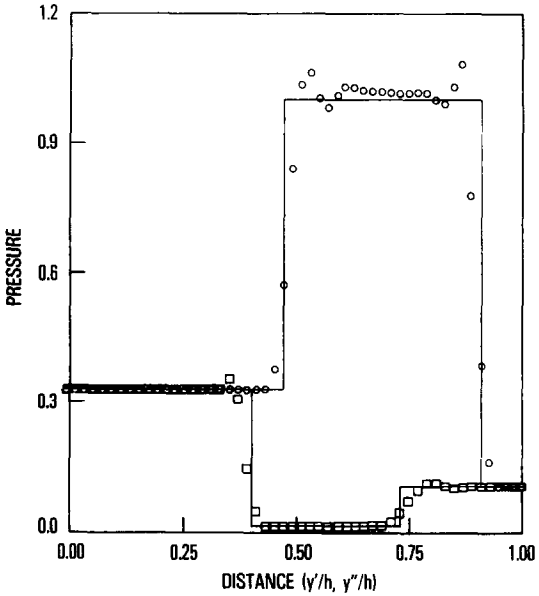

FIG. 18. The exact solutions and numerical results with the MacCormack scheme for the shock interaction problem defined in [17]. ○, Results at section $B-B$; □, results at section $A-A$. Solid lines are the exact solution.

obtain a given accuracy. We have not endeavored here to carry out as thorough a comparison here as that presented in [21], but a comparison of Figs. 17 and 18 indicates that the situation is similar. We also note that, unlike the MacCormack scheme, the high-order Godunov scheme does not contain a problem-dependent smoothing parameter which must be adjusted on a trial and error basis for each new problem.

ACKNOWLEDGMENTS

The authors would like to thank Jay Solomon for several helpful discussions during the preparation of this paper. This work was supported by the Naval Surface Weapons Center Independent Research Fund and the Naval Air Systems Command.

REFERENCES

1. M. E. SALAS, Shock fitting method for complicated two-dimensional supersonic flows, *AIAA J.* **14** (1976), 583–588.
2. A. B. WARDLAW, F. P. BALTAKIS, J. M. SOLOMON, AND L. B. HACKERMAN, An inviscid computational method for tactical missiles, *in* "Second Symposium on Numerical and Physical Aspects of Aerodynamic Flows," California State Univ., Long Beach, Jan. 1983.

3. J. M. SOLOMON, M. CIMENT, R. E. FERGUSON, J. B. BELL, AND A. B. WARDLAW, "A Program for Computing Steady Inviscid Three-Dimensional Supersonic Flow of Reentry Vehicles. Vol. I. Analysis and Programming," NSWC/WOL TR 77-28, Feb. 1977.
4. A. B. WARDLAW, F. P. BALTAKIS, J. M. SOLOMON, AND L. B. HACKERMAN, "An Inviscid Computational Method for Tactical Missile Configurations," NSWC TR 81-457, Dec. 1981.
5. S. M. DASH AND P. D. DELGUIDICE, Analysis of three dimensional ducted and exhaust plume flowfield, *AIAA J.* **16** (8) (Aug. 1978), 823–830.
6. P. COLELLA, "A Direct Eulerian MUSCL Scheme for Gas Dynamics," Lawrence Berkley Laboratory Report LBL-14104, 1982.
7. P. COLELLA AND P. R. WOODWARD, The piecewise-parabolic method (PPM) for gas-dynamical simulations, *J. Comput. Phys.* **54** (1984), 174–201.
8. P. COLELLA AND H. M. GLAZ, Numerical modeling of inviscid shocked flows of real gas, *in* "Proceedings, Eighth International Conference on Numerical Methods in Fluid Dynamics," Springer-Verlag, New York/Berlin, 1982.
9. P. COLELLA AND H. M. GLAZ, Efficient solution of the Riemann problem for real gases, *J. Comput. Phys.*, in press.
10. B. VAN LEER, Towards the ultimate conservative difference scheme. V. A second-order sequel to Godunov's method, *J. Comput. Phys.* **32** (1979), 101–136.
11. R. COURANT AND K. O. FRIEDRICHS, "Supersonic Flow and Shock Waves," Interscience, New York, 1948.
12. P. D. LAX, "Hyperbolic Systems of Conservation Laws and the Mathematical Theory of Shock Waves," SIAM, Philadelphia, 1972.
13. E. BECKER, "Gas Dynamics," Academic Press, New York/London, 1968.
14. H. W. LIEPMANN AND A. ROSHKO, "Elements of Gasdynamics," Wiley, New York, 1957.
15. G. MARSHALL AND B. PLOHR, A random choice method for two-dimensional steady supersonic shock wave diffraction problems, preprint, 1983.
16. S. K. GODUNOV, A difference method for numerical calculation of discontinuous solutions of the equations of hydrodynamics, *Mat. Sb.* **47** (1959), 271–306 (in Russian).
17. W. F. NOH, "Numerical Methods in Hydrodynamic Calculations," Lawrence Livermore National Laboratory Report UCRL-52112, 1976.
18. J. GOODMAN, "Initial Boundary Value Problems for Hyperbolic Systems of Conservation Laws," Center for Pure and Applied Mathematics, U.C. Berkeley Report PAM-99, 1982.
19. R. W. MACCORMACK, "The Effect of Viscosity in Hypervelocity Impact Cratering," AIAA Paper 69-534, Cincinnati, Ohio, 1969.
20. A. HARTEN AND G. ZWAS, Switched numerical Schuman filters for shock calculations, *J. Engrg. Math.* **2** (1972), 207–216.
21. P. WOODWARD AND P. COLELLA, "The Numerical Simulation of Two-Dimensional Fluid Flow with Strong Shocks," *J. Comput. Phys.* **54** (1984), 115–173.